IEEE Transactions on Robotics (T-RO) paper, presented at ICRA 2026, Vienna, Austria. Cite as T-RO paper.

FlowSight: Vision-Based Artificial Lateral Line Sensor for Water Flow Perception

Tiandong Zhang, *Member, IEEE*, Rui Wang, *Senior Member, IEEE*, Qiyuan Cao, *Student Member, IEEE*, Shaowei Cui, *Member, IEEE*, Gang Zheng, *Senior Member, IEEE*, and Shuo Wang, *Member, IEEE*

***Abstract*—This article presents a novel vision-based artificial lateral line (ALL) sensor, FlowSight, enhancing the perception capabilities of underwater robots. Through an autonomous vision system, FlowSight allows for simultaneous sensing the speed and direction of local water flow without relying on external auxiliary equipment. Inspired by the lateral line neuromast of fish, a flexible bionic tentacle is designed to sense water flow. Deformation and motion characteristics of the tentacle are modeled and analyzed using bidirectional fluid-structure interaction (FSI) simulation. Upon contact with water flow, the tentacle converts water flow information into elastic deformation information, which is captured and processed into an image sequence by the autonomous vision system. Subsequently, a water flow perception method based on deep neural networks is proposed to estimate the flow speed and direction from the captured image sequence. The perception network is trained and tested using data collected from practical experiments conducted in a controllable swim tunnel. Finally, the FlowSight sensor is integrated into the bionic underwater robot RoboDact, and a closed-loop motion control experiment based on water flow perception is conducted. Experiments conducted in the swim tunnel and water pool demonstrate the feasibility and effectiveness of FlowSight sensor and the water flow perception method.**

Received 22 November 2024; revised 20 February 2025; accepted 21 April 2025. Date of publication 6 May 2025; date of current version 23 May 2025. This work was supported in part by the STI 2030—Major Projects under Grant 2022ZD0209600, in part by the National Natural Science Foundation of China under Grant 62403463, Grant 62276253, Grant 62203435, and Grant U23B2038, in part by the Postdoctoral Fellowship Program of CPSF under Grant GZC20241917, and in part by the China Postdoctoral Science Foundation under Grant 2024M763532. This article was recommended for publication by Associate Editor M. Kim and Editor S. Behnke upon evaluation of the reviewers' comments. *(Corresponding author: Rui Wang.)*

Tiandong Zhang, Rui Wang, and Shaowei Cui are with the State Key Laboratory of Multimodal Artificial Intelligence Systems, Institute of Automation, Chinese Academy of Sciences, Beijing 100190, China (e-mail: tiandong.zhang@ia.ac.cn; rwang5212@ia.ac.cn; shaowei.cui@ia.ac.cn).

Qiyuan Cao is with the State Key Laboratory of Multimodal Artificial Intelligence Systems, Institute of Automation, Chinese Academy of Sciences, Beijing 100190, China, and also with the School of Artificial Intelligence, University of Chinese Academy of Sciences, Beijing 100049, China (e-mail: caoqiyuan2021@ia.ac.cn).

Gang Zheng is with the Centrale Lille, CRIStAL - Centre de Recherche en Informatique Signal et Automatique de Lille, University of Lille, 59000 Lille, France (e-mail: gang.zheng@inria.fr).

Shuo Wang is with the State Key Laboratory of Multimodal Artificial Intelligence Systems, Institute of Automation, Chinese Academy of Sciences, Beijing 100190, China, also with the School of Artificial Intelligence, University of Chinese Academy of Sciences, Beijing 100049, China, and also with the Center for Excellence in Brain Science and Intelligence Technology, Chinese Academy of Sciences, Shanghai 200031, China (e-mail: shuo.wang@ia.ac.an).

This article has supplementary downloadable material available at https://doi.org/10.1109/TRO.2025.3567551, provided by the authors.

Digital Object Identifier 10.1109/TRO.2025.3567551

***Index Terms*—Artificial lateral line (ALL), biomimetic, robot environment perception, vector measurement, water flow perception.**

I. Introduction

UNDERWATER flow field perception is essential for navigation, positioning, collaboration, and various other tasks performed by underwater robots [1], [2], particularly in challenging underwater environments characterized by low illumination and significant external disturbances [3], [4]. Such perception capabilities empower robots to enhance their environmental awareness and accomplish underwater tasks with greater efficiency. Consequently, enhancing the ability to perceive flow fields has emerged as a pivotal research focus within the field of underwater robots, offering promising avenues for practical application.

In the natural world, fish primarily rely on their lateral line system to perceive their surroundings and gather information about the underwater flow field [5], [6]. Biologists have demonstrated the indispensable role of the lateral line system in various fish behaviors, including obstacle avoidance, predation, positioning, and collective swimming [7]. Drawing inspiration from this biological mechanism, researchers have developed a range of artificial lateral line (ALL) sensors to sense the flow field and underwater environment [8]. These ALL sensors can detect and measure various environmental parameters, such as water pressure, flow velocity, and turbulence, which are crucial for navigating complex underwater environments and performing precise measurements. The ALL sensor is the key to improve the practicability and intelligence of underwater robots. Over the last decade, numerous ALL sensors have been developed. Some state-of-the-art ALL sensors are delineated in Table I. These sensors can be broadly categorized into two types based on their bionic principles and manufacturing methods: Structural bionic ALL sensors and functional bionic ALL sensors [9], [10].

Inspired by the tentacle structure of fish lateral line neuromast, structural bionic ALL sensors with tentacle-like features have been developed using advanced microelectro-mechanical system (MEMS) manufacturing technologies such as micro processing, photolithography, and film deposition. Upon contact with fluid, these sensors convert flow field information into deformation data via their tentacle-like structures. Consequently, water flow can be detected by measuring this deformation with various sensing methods including piezoresistance,

TABLE I
COMPARISON OF THE PROPOSED FLOWSIGHT SENSOR WITH THE EXISTING STATE-OF-THE-ART ALL SENSORS

Sensor	Bionic Type	Speed Measurement	Direction Measurement	Advantages	Limitations
Zhang [8]	Structural	Range: $0-0.4$ m/s Error: 4.1%	Range: full Error: 10.6°	Hardware-based noise suppression	Subpar dynamic performance, large sensor array
Abels [11]	Structural	Range: $0.2-50$ m/s Error: 15%	Range: positive or negative Error: unknown	Real-time measurement	Insensitivity to low speed
Wolf [12]	Structural	Range: >0.05 m/s Error: 10.8%	Range: full Error: 1.8°	High angular sensitivity	Complicated signal processing, large volume
Xie [3]	Functional	Range: $0-0.2$ m/s Error: 3.62%	Range: full Error: 14.4°	Hydrodynamic pressure variation model	Large sensor array
Fuentes-Pérez [13]	Functional	Range: $0-2$ m/s Error: 0.54%	Incapable	High sampling rate of speed	Additional correction for low speed
Zhu [14]	Functional	Incapable	Range: full Error: 4.61°	Data-driven method	Ideal condition assumption
FlowSight (ours)	Structural	Range: $0.325-0.715$ m/s Error: 3.05%	Range: full Error: 3.54°	Simultaneous exact sensing of speed and direction of local flow	Precision limited by the datasets

piezoelectricity, optics, and others. Abdulsadda and Tan [15] developed a structural bionic ALL sensor based on a flexible cantilever beam by using the piezoelectric effect of ionic metal polymer composites. The perceived stress variations are directly translated into electric current via the piezoelectric sensor, enhancing the sensitivity of the ALL sensor. Nevertheless, this material exhibits unstable performance and imposes stringent environmental requirements. Abels et al. [11] designed a sensor using a stack of silicon nitride/silicon layers, fixed to a substrate to form a cantilever beam. The stress differences between the layers generate a stress gradient, causing the cantilever to bend under fluid forces. The bending induces changes in the resistance of the strain gauge due to the resulting stress variations. As a result, the local flow velocity is determined from the voltage variations across the strain gauge terminals. The sensor offers a broad measurement range for velocity, spanning from 0.2 m/s to 50 m/s, but its measurement accuracy is limited, making it challenging to meet precise control requirements.

Due to the limitation of the structure and measurement method, most of these structural bionic ALL sensors using cantilever structure can only measure the water flow speed in a fixed direction without sensing the water flow direction. The array of multiple sensors need to be established to measure flow direction using data fusion processing techniques. Zhang et al. [8] developed an ALL sensor based on cantilever structure. A pair of resistance strain gauges are symmetrically pasted on a fixed plane made of aluminum alloy. When the fixed plane is impacted by water flow, the strain gauge transforms the strain force into current change to realize water flow perception. Eight ALL sensors are assembled as a sensor array to sense the water flow direction. Different from cantilever structure, Liu et al. [16] developed a structural bionic ALL sensor based on optics for 2-D velocity measurement, which can measure the speed and direction of water flow at a single point. The shear stress generated by the contact between the fluid and the sensor drives the cylinder's tentacle to bend. The deformation of the cylinder's tentacle is observed and captured by an external high-speed camera. Shear stress is computed through analysis of the 2-D displacement variation at the sensor's apex, subsequently enabling estimation of the speed and direction of the local flow field. Moreover, Wolf et al. [12], [17] designed an optical ALL sensor for 2-D velocity measurement, which consists of a stress sphere and a fiber with the Bragg grating. The spectral analysis is carried out using an external bulky optical inquiry device to realize the simultaneous measurement of water flow speed and direction.

In recent years, to streamline the manufacturing process of ALL sensors and enhance stability, researchers have started to mimic the functionality of fish lateral lines. They utilize commercially mature technologies such as pressure measurement to achieve water flow perception. Zheng et al. [3] used a group of commercial pressure sensors to form an ALL system to imitate the sensing function of fish lateral line on pressure. In total, 11 commercial pressure sensors are evenly arranged on both sides of the bionic robot fish to measure the pressure distribution on the robot's surface in the flow. The inertial measurement unit is used to calibrate the measurement of the ALL sensor. However, pressure sensors solely capture absolute pressure, posing challenges in discerning minute pressure variations amidst substantial static pressure in deep water. Consequently, it is difficult to distinguish the pressure change caused by water flow and noise, resulting in increased measurement error. In order to overcome the shortcomings of the absolute pressure sensor, Fuentes-Pérez et al. [13] developed a functional bionic ALL sensor based on the differential pressure sensor. The differential pressure sensor is used as the basic unit of the ALL sensor, mitigating absolute pressure interference due to water depth and enhancing the stability and accuracy of flow speed measurement. Zhu et al. [14] arranged a linear array of differential pressure sensors, and employed the data-driven neural network approach to

achieve highly accurate flow direction estimation. Nonetheless, the absolute pressure at the differential pressure sensor's input end must not exceed its upper limit, thereby constraining the sensor's operational depth.

In conclusion, despite extensive research efforts in the field of ALL sensors, the extant ALL sensors still face several challenges in practical applications, impeding their effective integration into bionic underwater robots. Structural bionic ALL sensors exhibit the capability to detect local water flow information with small dimensions and high flexibility. However, these sensors suffer from complexities in manufacturing processes, susceptibility to pollution (MEMS), bulky equipment volume (optical principle), and limited stability. In addition, functional bionic ALL sensors exhibit robust stability, simple manufacturing processes, and affordability. However, these sensors require array formation for sensing, which is significantly impacted by depth (pressure sensor) and poses challenges in detecting local water flow information. Furthermore, there are few ALL sensors that can simultaneously sense both the speed and direction of local water flow, further constraining their application scenarios and perception capabilities. Designing a compact ALL sensor with high efficiency, stability, simplified manufacturing processes, and cost-effectiveness is crucial for enhancing the practicality of ALL sensors.

In response to the previously mentioned challenges, this article proposes a vision-based bionic ALL sensor called FlowSight, which can detect local water flow and simultaneously estimate flow speed and direction at the measuring site. Drawing inspiration from the structure of fish lateral line neuromast, we have devised a flexible bionic tentacle to convert water flow information into geometric deformations of elastic materials. Moreover, these deformations are captured by a high-definition camera integrated within the sensor. Subsequently, leveraging the visual image sequences of the fluid-solid interface, a water flow perception method is proposed for simultaneous estimation of local flow speed and direction, utilizing convolutional neural networks (CNN) and long short-term memory (LSTM) networks. It allows for the estimation and extraction of water flow information contained in image features, facilitated by supervised learning with deep neural networks. The FlowSight can sense the vector velocity information of local water flow efficiently and stably, which is crucial for underwater robots navigation and accurate measurement in complex underwater environment.

The main contributions of this article are given as follows.

1) Principle and implementation of a novel bionic ALL sensor (FlowSight) based on autonomous vision, which can simultaneously sense the local flow direction and speed information within the flow field. Specifically, the FlowSight independently uses its own visual system to perceive and comprehend the environment without relying on external auxiliary equipment.
2) End-to-end artificial neural network processing approach, realizing direct perception of flow vector velocity from visual images. The water flow perception network of FlowSight is trained and tested through supervised learning in a controllable velocity swim tunnel, where the flow speed and direction can be directly obtained and changed.
3) Practical validation of the developed FlowSight sensor on a bionic underwater robot prototype, which demonstrates the feasibility and effectiveness of the FlowSight sensor in practical applications. To the best of the authors' knowledge, the closed-loop motion control of bionic underwater robot in water pool based on water flow perception is realized for the first time.

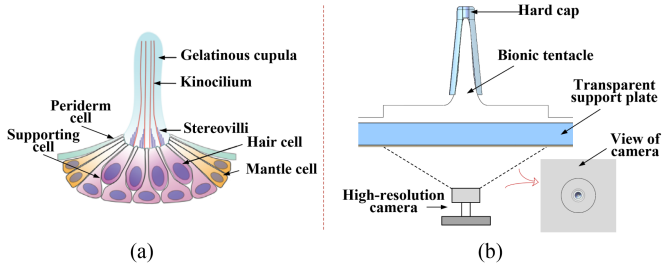

Fig. 1. Schematic diagram of the lateral line neuromast. (a) Fish lateral line neuromast. (b) Biomimetic lateral line neuromast of FlowSight.

The rest of this article is organized as follows. Section II illustrates the design and fabrication of the proposed ALL sensor FlowSight. In Section III, the deformation model and fluid-structure interaction (FSI) simulation are employed to analyze the deformation and movement characteristics of the FlowSight's flexible bionic tentacle under the water flow. In Section IV, a water flow perception method is proposed based on CNN-LSTM, enabling simultaneous estimation of local flow speed and direction. Section V describes the experiments and analysis. Experiments on water flow perception using FlowSight are conducted in a controllable velocity swim tunnel. In addition, the developed FlowSight sensor is integrated into a bionic underwater robot RoboDact prototype [18], which is utilized for closed-loop motion control based on water flow perception. The feasibility and effectiveness of the FlowSight are demonstrated. Finally, Section VI concludes this article and summarizes future work.

II. Design and Fabrication of the FlowSight

In nature, fish predominantly depend on their lateral line system to acquire information about the underwater flow field and perceive the surrounding aquatic environment. The lateral line neuromast functions as the primary sensory unit for the mechanical perception of fish lateral line systems [6], [19]. Illustrated in Fig. 1(a), the lateral line neuromast primarily comprises four types of cells: hair cells, periderm cells, supporting cells, and mantle cells. Hair cells are responsible for detecting mechanical vibration waves. Upon detection of mechanical stimuli caused by water flow, hair cells convert these stimuli into neurophysiological signals, which are then transmitted to the central nervous system. Periderm cells serve a protective function for the lateral line neuromast. In addition, supporting cells and mantle cells are crucial for the regeneration and repair of hair cells. These cells can secrete a double-layered gelatinous

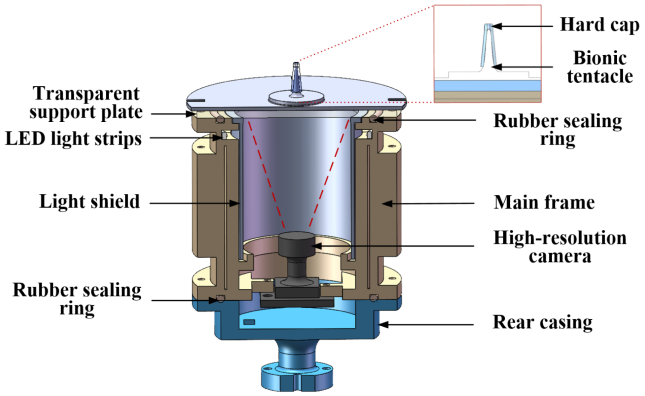

Fig. 2. Schematic diagram of the FlowSight's mechanism design.

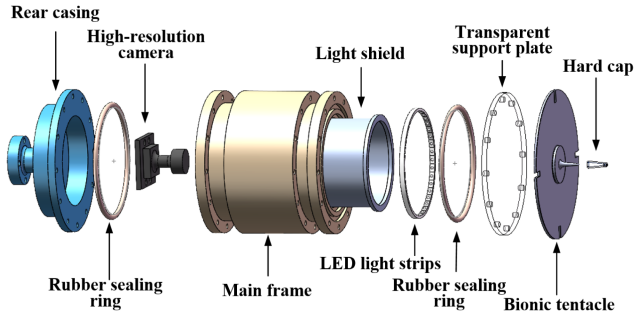

Fig. 3. Exploded view of the FlowSight.

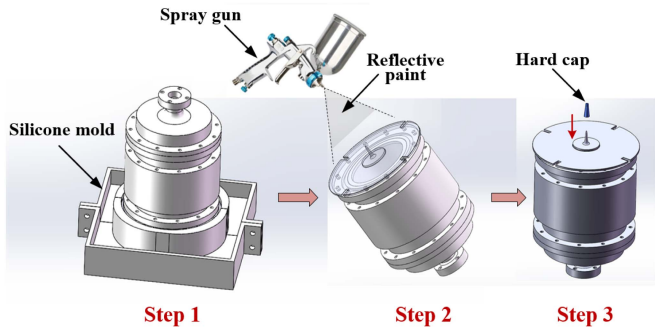

Fig. 4. Fabrication process of the FlowSight.

cupula, which protects the hair cells and facilitates the deflection of the ciliary bundle. The sensory unit of the hair cells in the neuromast comprises kinocilia and stereocilia, consisting of kinocilium and stereovilli, respectively [19]. Upon experiencing fluid stimulation from a specific direction, the movement of the gelatinous cupula drives the deflection of the ciliary bundle in a specific orientation, leading to alterations in the intracellular and extracellular potential of the hair cells. This process generates neurophysiological signals, which are transmitted via afferent nerves to the central nervous system. Finally, fish process these electrical signals in the central nervous system to perceive the water flow around the body.

A. Mechanical Design

By imitating the neural structure of fish lateral line neuromast, a novel vision-based ALL sensor called FlowSight is designed, which enables simultaneous estimation of local flow speed and direction. FlowSight aims to enhance the underwater perception capabilities of underwater robots. The fundamental sensing principle of the FlowSight is illustrated in Fig. 1(b). An isotropic flexible bionic tentacle is located at top of the sensor to contact with external water flow, transforming flow data into geometric deformations within the elastic material. Subsequently, a high-resolution camera, housed within the sensor, records the induced deformations in the form of an image sequence. Lastly, the captured image sequence undergoes analysis through the proposed water flow perception method, where the developed perception network enables simultaneous estimation of both flow speed and direction.

The structure of the FlowSight is similar to the lateral line neuromast in fish, as shown in Fig. 2. By imitating structure and function of the hair cells found in the lateral line neuromast of fish, a transparent silicone rubber bionic tentacle is deployed to interact with water flow and undergo deformation, enabling water flow sensing. Mimicking the protective role of the gelatinous cap, a uniform layer of silver reflective paint is sprayed on the silicone rubber surface, serving to safeguard the sensor while preventing external light infiltration, thus ensuring a stable internal light environment within the sensor. Furthermore, a resin-made hard cap encases the outer layer of the bionic tentacle, providing additional protection, which can also amplify the deformation by inducing deviations in the bionic tentacle. Analogous to the supporting cells, a transparent acrylic support plate is positioned beneath the bionic tentacle, providing support to the silicone rubber layer.

Fig. 3 shows an exploded view of the FlowSight sensor. The main frame serves as the central support structure for mounting diverse components, while the rear casing can feature versatile interfaces to adapt to various application scenarios. Fasteners are utilized to secure the rear casing, main frame, and transparent acrylic support plate together, with rubber sealing rings ensuring an airtight seal between components to maintain the sensor's interior dryness and integrity. Adjacent to the transparent support plate, a circular arrangement of light-emitting diode (LED) light strips is deployed to produce a dense light source, complemented by a light shield to generate a uniform light environment within the sensor. Located beneath the sensor, a high-resolution camera is precisely directed toward the underside of the bionic tentacle to capture real-time tentacle deformation. Finally, the captured images undergo processing via the water flow perception neural network to enable simultaneous estimation of flow speed and direction.

B. Fabrication Process

After the main structure of the FlowSight is assembled, the bionic tentacle of the sensor is made as shown in Fig. 4. First, 3-D printing mold and the smooth baseplate are assembled to form the silicone mold. The main structure of the FlowSight is

TABLE II
TECHNICAL PARAMETERS OF THE FLOWSIGHT

Parameters	Value	Parameters	Value
Diameter of the body	57.0 mm	Height of the bionic tentacle with cap	10 mm
Height of the body	53.8 mm	Measurement range of flow speed	$32.5 - 71.5$ cm/s
Total mass	0.05 kg	MAE of speed measurement	1.1903 cm/s
Total gravity	0.5 N	Relative error of speed measurement	3.05%
Total buoyancy	0.3 N	Measurement range of flow direction	$0 - 360°$
Diameter of the tentacle's top	1 mm	MAE of direction measurement	3.5407°
Diameter of the tentacle's bottom	4 mm	Relative error of direction measurement	0.98%

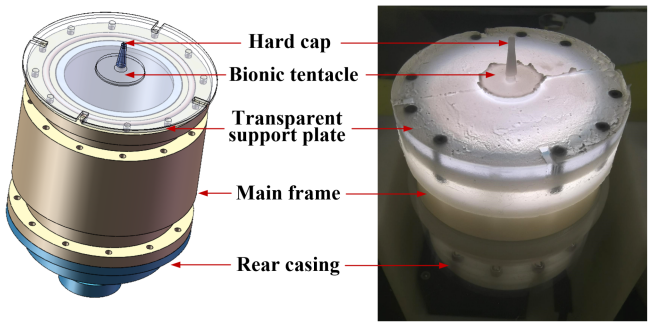

Fig. 5. 3-D model and a prototype of the FlowSight sensor.

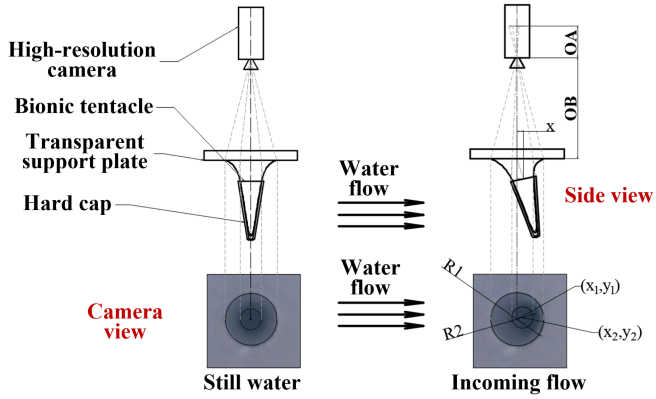

Fig. 6. Schematic diagram of the relationship between tentacle deflection and incoming flow.

then placed into the mold and secured, as detailed in Step 1 of Fig. 4. The transparent silicone rubber material is mixed in a certain ratio and poured into the silicone mold, where it cures at room temperature. Using the mold flipping technique, the flexible transparent silicone tentacle and the transparent silicone base layer are formed. Next, as described in Step 2 of Fig. 4, a light-blocking gel spray material is prepared by mixing gel adhesive, silver reflective paint, and diluent in a specific ratio for the creation of the gel protective layer. This material is evenly sprayed onto the surface of the flexible tentacle and the flexible base layer using a spray gun, forming the gel protective layer, which provides a stable internal light field environment. As illustrated in Step 3 of Fig. 4, the hard cap is fabricated using resin material through 3-D printing technology. It is then fixed to the outer side of the flexible tentacle with a gel adhesive, serving to protect the sensing tentacle and enhance their sensitivity.

Based on the design of the FlowSight sensor as described above, the physical prototype has been developed as presented in Fig. 5. Table II provides some technical parameters for the sensor.

III. MODELING AND SIMULATION OF FLOWSIGHT'S FLEXIBLE BIONIC TENTACLE

The flexible bionic tentacle, a crucial sensing element, is designed to convert water flow information into geometric deformation. The tentacle deflects within the vertical plane due to the impact of water flow, which is manifested in the image as a displacement of the central shadow feature. The schematic diagram is shown in Fig. 6. To quantitatively characterize the input-output relationship of bionic tentacle, a deformation model of the flexible tentacle is developed. In addition, an FSI simulation is crafted to scrutinize motion traits of the tentacle amidst water flow.

A. Deformation Model of the Tentacle

Within the fish's lateral line system, the movement of superficial neuromast is encoded as changes in the action potential frequency in transmitting neurons [6]. These signals provide information about the water flow around the body to the central nervous system. According to previous studies [19], [20], the resistance in static conditions primarily comes from the bending stiffness and the torsional restoring constant of the cilia. In non-static conditions, the deflection of this structure is determined by the coupled structural mechanics between cilia and the fluid's fluid dynamics properties.

As described in Section II, the flexible bionic tentacle of the FlowSight is designed to interact with water flow, translating flow information into deformation data. Hence, a deformation model is formulated to elucidate the impact of water flow on the deflection angle of the bionic tentacle. The water flow detected by the bionic tentacle is subject to fluid dynamics, as depicted in Fig. 7. The viscosity of water induces slower flow within a thin layer near the contact surface compared to free flow. Within the boundary layer, fluid velocity experiences a gradual increase from near-zero at the surface to the free-stream velocity [21].

In a free and constant water flow, the fluid velocity u_y near the contact surface can be represented as follows:

$$u_y = u(y) = \begin{cases} u_0 & , \text{if } y > \delta \\ u_0 \cdot \left(\frac{2y}{\delta} - \frac{y^2}{\delta^2}\right) & , \text{if } 0 < y < \delta \end{cases} \quad (1)$$

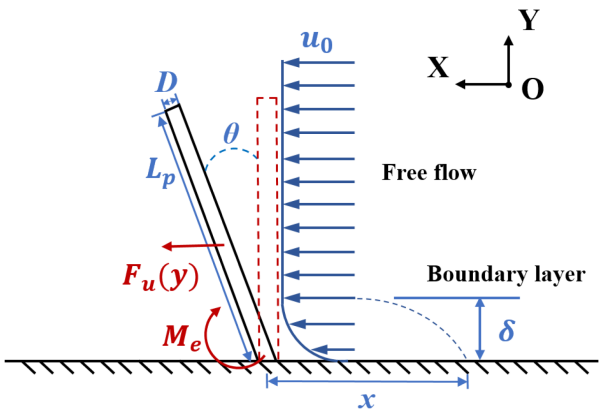

Fig. 7. Schematic diagram of the bionic tentacle deflection in water flow.

where u_0 is the free flow velocity, y is the distance from the contact surface to the measurement position, and the boundary layer thickness δ can be calculated as follows:

$$\delta = \frac{5}{\sqrt{Re_x}}x \tag{2}$$

where x represents the distance from the current position to the leading edge, and Re_x is the local Reynolds number, which satisfies $Re_x = \rho u_0 x/\mu$. Here, ρ is the density of water, and μ is the dynamic viscosity.

The flexible bionic tentacle is designed as an axisymmetric structure, endowing it with isotropic properties in water flow. To facilitate analysis and simplify calculations, tentacle displacement in the flow direction is contemplated, as illustrated in Fig. 7. Thus, under laminar steady-state flow conditions, the 2-D deformation model of the tentacle is investigated, without accounting for the influence of a vibration source. In laminar steady-state flow, the tentacle experiences predominant effects from the viscous drag force exerted by water F_u and its intrinsic elastic restoring force F_e [22]. Under steady-state conditions, they satisfy $F_u(y) = F_e(y)$. Furthermore, the moment generated at the tentacle's base due to the water force is denoted as M_u, which equals the elastic recovery torque of the tentacle M_e.

$$M_u = M_e. \tag{3}$$

The local viscous drag force from water $F_u(y)$ can be calculated as follows:

$$\begin{aligned} F_u(y) &= \frac{1}{2}\rho C_D D {u_y}^2 \mathrm{d}y \\ F_u &= \int_0^{L_p} \mathrm{d}F_u(y) \\ &= \frac{1}{2}\rho C_D D \int_0^{L_p} {u_y}^2 \mathrm{d}y \\ &= \frac{1}{2}\rho C_D D \left[\int_0^{\delta} {u_0}^2 \left(\frac{2y}{\delta} - \frac{y^2}{\delta^2}\right)^2 \mathrm{d}y + \int_{\delta}^{L_p} {u_0}^2 \mathrm{d}y\right] \\ &= \frac{1}{2}\rho C_D D {u_0}^2 \left[\int_0^{\delta} \left(\frac{2y}{\delta} - \frac{y^2}{\delta^2}\right)^2 \mathrm{d}y + (L_p - \delta)\right] \end{aligned} \tag{4, 5}$$

where C_D is the dimensionless drag coefficient, and D is average diameter of the tentacle. Therefore, the moment generated by viscous drag force from water M_u can be calculated as follows:

$$\begin{aligned} M_u &= \int_0^{L_p \cos\theta} y \, \mathrm{d}F_u(y) \\ &= \frac{1}{2}\rho C_D D {u_0}^2 \cos^2\theta \left[\int_0^{\delta} \left(\frac{2y}{\delta} - \frac{y^2}{\delta^2}\right)^2 y \mathrm{d}y \right. \\ &\quad \left. + \int_{\delta}^{L_p} y \mathrm{d}y\right] \\ &= \frac{1}{2}\rho C_D D {u_0}^2 \cos^2\theta \left[\int_0^{\delta} \left(\frac{2y}{\delta} - \frac{y^2}{\delta^2}\right)^2 y \mathrm{d}y \right. \\ &\quad \left. + \frac{{L_p}^2 - \delta^2}{2}\right]. \end{aligned} \tag{6}$$

The outer side of the bionic tentacle, encased in a rigid resin-made hard cap, is approximately treated as a model of hair deformation [23]. Specifically, the tentacle is considered a rigid structure, while the bottom contact surface is simplified as a spring and damping system. Therefore, the tentacle deformation can be represented by the tentacle deflection θ. Through the projection on the imaging plane, the deflection caused by the impact of water flow is transformed into a displacement in the central shadow feature. The relationship between the deflection angle θ and the elastic recovery torque M_e of the tentacle can be expressed as follows:

$$M_e = I\ddot{\theta} + R\dot{\theta} + S\theta \tag{7}$$

where I denotes the moment of inertia of the tentacle (approximated as a rigid body) relative to its rotational center. θ stands for the angular displacement of the tentacle around its joint. R denotes the damping constant or frictional resistance. S represents the torsional spring constant that restores the bent tentacle to its resting position. For ease of analysis, consider the tentacle in a steady-state condition, where the values of $\ddot{\theta}$ and $\dot{\theta}$ are both equal to 0. Therefore, (7) can be simplified as follows:

$$\begin{aligned} S \cdot \theta &= M_e \\ &= M_u \\ &= \frac{1}{2}\rho C_D D {u_0}^2 \cos^2\theta \left[\int_0^{\delta} \left(\frac{2y}{\delta} - \frac{y^2}{\delta^2}\right)^2 y \mathrm{d}y \right. \\ &\quad \left. + \frac{{L_p}^2 - \delta^2}{2}\right]. \end{aligned} \tag{8}$$

When the boundary layer δ is small, the (8) can be simplified as follows:

$$\frac{\theta}{\cos^2\theta} \approx \frac{1}{4S}\rho C_D D L_p^2 u_0^2. \tag{9}$$

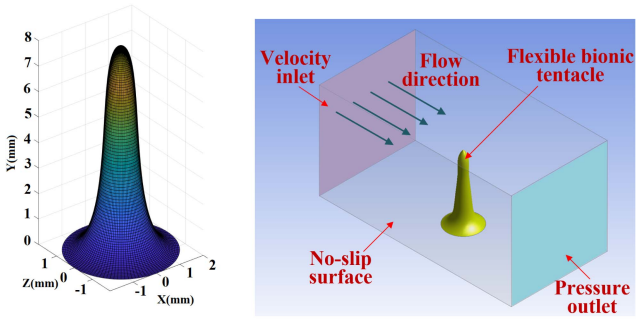

(a) (b)

Fig. 8. Simulation model of the FlowSight. (a) Surface profile of the tentacle. (b) Flow field model.

Moreover, the relationship between the deflection angle θ of the tentacle and the pixel displacement d' in the image is shown as follows. Under the action of water flow, the FlowSight's hard cap drives the tentacle to deflect. The displacement of the bottom of the hard cap is represented as d. The following formula can be obtained from the geometric relationship:

$$d = L_1 \sin\theta \tag{10}$$

where L_1 denotes the distance from the bottom of the hard cap to the bottom of the tentacle. Based on camera's optical imaging model, the pixel distance d' on the image is related to the actual distance d as follows:

$$\frac{d}{d'} = \frac{L_0}{f} \tag{11}$$

where L_0 is the distance between the tentacle base and the camera, and f represents the focal length. Therefore, the relationship between the deflection angle θ and the pixel displacement d' can be expressed as follows:

$$d' = \frac{L_1 f}{L_0} \sin\theta. \tag{12}$$

Through the tentacle deformation, the FlowSight can transfer the water flow information into a displacement in the central shadow feature on the imaging plane.

B. FSI Simulation of the Tentacle

To further analyze the deformation and motion characteristics of the tentacle under the influence of water flow, a bidirectional FSI simulation is developed using computational fluid dynamics (CFD) technology.

By mimicking the "narrower upper part and wider lower part" configuration of the biological lateral line neuromast, the structure of the FlowSight bionic flexible tentacle is designed, as illustrated in Fig. 8(a). The thinner upper part enhances sensitivity to perception, while the thicker lower part increases stability. To ensure a seamless transition and maintain a smooth tentacle surface between the two parts, the surface profile of the tentacle is generated using a cubic Bézier curve [24]. The surface curve equation can be expressed as follows:

$$\begin{cases} x = [(1-\beta)^3 P_0(x) + 3\beta(1-\beta)^2 P_1(x) \\ \qquad +3\beta^2(1-\beta)P_2(x) + \beta^3 P_3(x)] \cdot \cos(\alpha) \\ y = (1-\beta)^3 P_0(y) + 3\beta(1-\beta)^2 P_1(y) \\ \qquad +3\beta^2(1-\beta)P_2(y) + \beta^3 P_3(y) \\ z = [(1-\beta)^3 P_0(x) + 3\beta(1-\beta)^2 P_1(x) \\ \qquad +3\beta^2(1-\beta)P_2(x) + \beta^3 P_3(x)] \cdot \sin(\alpha) \end{cases} \tag{13}$$

where the Bézier curve parameters are given by $\beta \in [0, 1]$ and the rotation angle is denoted by $\alpha \in [0, 2\pi]$. The four positioning points on the Bézier curve, $P = [x, y, z]$, are defined as follows: $P_0 = [0, h, 0]$, $P_1 = [0.25d, h, 0]$, $P_2 = [0, 0, 0]$, and $P_3 = [0.5d, 0, 0]$. In addition, the height of the tentacle is $h = 8$ mm, and the width (i.e., the bottom diameter) of the tentacle is $d = 4$ mm.

In FSI simulation, the interaction between the fluid and solid components is considered, where the fluid influences the shape, motion, and stress distribution of the solid, and vice versa. Initially, a geometric model is constructed based on the designed flexible bionic tentacle. Subsequently, a CFD simulation model is developed using this geometric foundation, as depicted in Fig. 8(b). The fluid inlet is assigned a velocity inlet boundary condition, while the fluid outlet is set as a pressure outlet boundary condition. In addition, the lateral boundaries of the fluid domain are defined as no-slip surface boundary conditions. The material properties of the bionic tentacle are modeled using silicone rubber, and the tentacle is anchored at its bottom using a no-slip surface boundary condition.

Next, the solid mesh and flow field mesh are generated. Based on the constructed geometric model of the tentacle, the solid mesh is created. A triangular mesh with a maximum mesh size of 0.2 mm is applied to the surface. After mesh smoothing and refinement, a total of 129 818 tetrahedral and triangular elements are generated, indicating high-quality meshing suitable for simulating the motion of the tentacle under external forces. Subsequently, building upon the solid mesh, a tetrahedral mesh for the flow field is generated. After mesh smoothing and refinement, the maximum mesh size is set to 1 mm, resulting in a total of 74 439 tetrahedral and triangular elements. The mesh quality remains high, facilitating a realistic simulation of the flow field variations around the bionic tentacle.

After completing the meshing, a bidirectional FSI simulation is conducted using the partitioned method. In this approach, the fluid and solid domains are solved separately by their respective solvers, and information is exchanged through the interface between them. During each time iteration of the simulation, the solid calculation part is restrained when simulating the fluid. The fluid module calculates the pressure and viscous forces at the fluid-solid interface and transfers the force information to the solid module. Conversely, the fluid calculation part is restrained when simulating the solid. The solid module computes the deformation and velocity of the solid based on the applied forces and transfers the deformation information to the fluid module. This iterative exchange continues until simulation completion.

Utilizing the CFD-based numerical modeling of the flexible bionic tentacle described above, bidirectional FSI simulations are performed with a simulation time of 2.0 s and a time step of

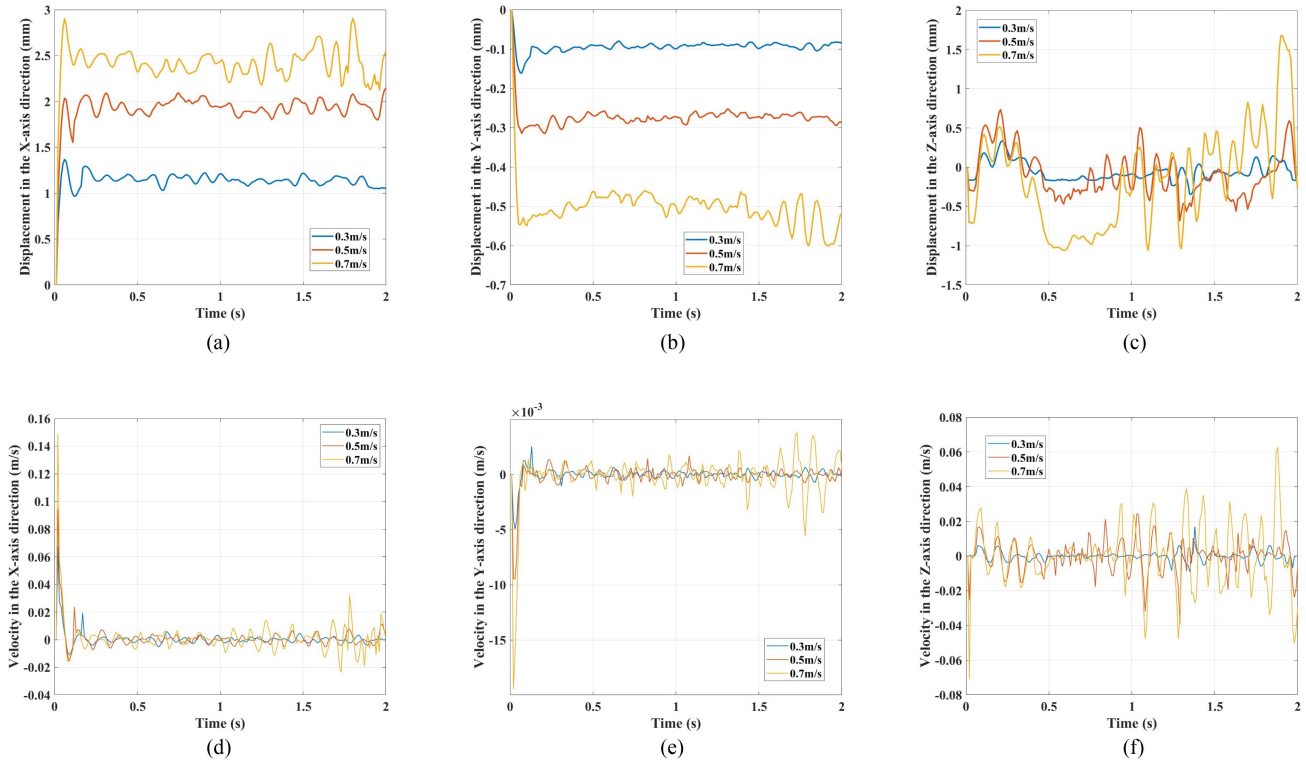

Fig. 9. Position changes and velocity changes of the monitoring point at different flow speeds. (a) Position changes at *X*-axis direction. (b) Position changes at *Y*-axis direction. (c) Position changes at *Z*-axis direction. (d) Velocity changes at *X*-axis direction. (e) Velocity changes at *Y*-axis direction. (f) Velocity changes at *Z*-axis direction.

0.01 s each time. Due to the axisymmetric and isotropic nature of the tentacle in the water flow direction, the flow direction remains fixed in this numerical simulation. To investigate the deformation and motion of the tentacle under different flow speeds, velocities of 0.3 m/s, 0.5 m/s, and 0.7 m/s are set separately. For ease of data processing and analysis, the vertex of the tentacle is chosen as the monitoring point. The position displacement and velocity of the monitoring point are recorded throughout the simulation process.

Based on the bidirectional FSI simulation results, an exploration and analysis of the motion and deformation of the bionic tentacle under the influence of water flow are conducted. The position displacement of the monitoring point under different flow speeds is illustrated in Fig. 9(a)–(c). After being impacted by the constant velocity water flow, the monitoring point exhibits significant displacement in the *X*-axis direction within a short time, maintaining this displacement while oscillating within a small range thereafter. In the *Y*-axis direction, the monitoring point experiences minor displacement initially, followed by relative stability. Regarding the *Z*-axis direction, the monitoring point undergoes significant oscillations around its initial position. The position displacement of the monitoring point is positively correlated with the water flow speed, with higher flow speeds resulting in larger displacement and oscillation amplitudes. At a flow speed of 0.7 m/s, the displacement of the monitoring point in the *X*-axis direction reaches approximately 2.5 mm, while in the *Y*-axis direction, it is around -0.5 mm. In the *Z*-axis direction, the displacement oscillates back and forth with a maximum amplitude of 1.5 mm. At a flow speed of 0.5 m/s, the displacement of the monitoring point in the *X*-axis direction is around 1.9 mm, in the *Y*-axis direction is around -0.3 mm, and in the *Z*-axis direction, it oscillates back and forth with a maximum amplitude of 0.7 mm. At a flow speed of 0.3 m/s, the displacement of the monitoring point in the *X*-axis direction is around 1.1 mm, in the *Y*-axis direction is around -0.1 mm, and in the *Z*-axis direction, it also undergoes smaller oscillations with a maximum amplitude of 0.3 mm.

The velocity variation of the monitoring point throughout the simulation process is depicted in Fig. 9(d)–(f). After 0.1 s of water flow impact, the flexible bionic tentacle stabilizes. Notably, the monitoring point's velocity shows small amplitude periodic oscillations centered around 0 in both the *X*- and *Y*-axis directions. However, significant fluctuations are observed in the *Z*-axis direction due to the formation of vortices on either side of the tentacle as water flows around it. These vortices induce uneven and periodic force variations, leading to relatively large fluctuations in the *Z*-axis direction.

Upon contacting the constant water flow, the pressure distribution on the surface of the flexible bionic tentacle is shown in Fig. 10, where the left side represents the side view of the bionic tentacle, and the right side represents the top view. The flow field direction goes from left to right. It can be observed that the bionic tentacle exhibits a noticeable and constant pressure difference on both front and rear surfaces along the *X*-axis direction at different time intervals. The pressure difference leads to significant displacement of the bionic tentacle in the

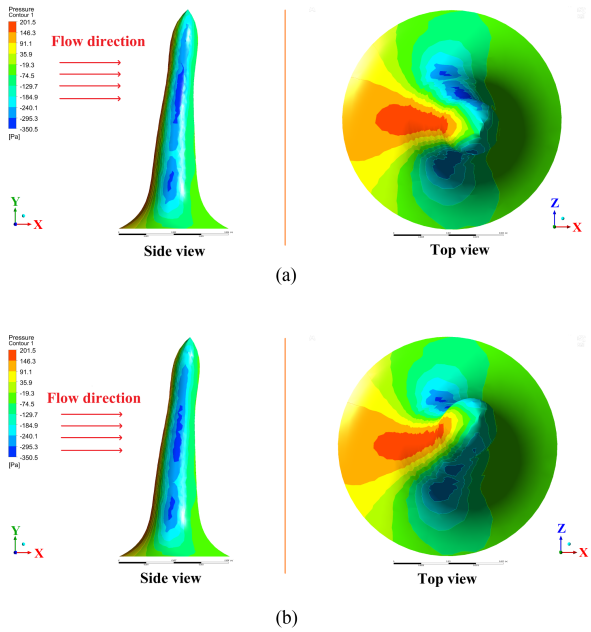

Fig. 10. Pressure distribution on the surface of the bionic tentacle. (a) Moment I. (b) Moment II.

water flow direction. Owing to the structural characteristics of the flexible bionic tentacle, the substantial displacement along the *X*-axis direction also engenders a minor displacement along the Y-axis direction. In the Z-axis direction, following interaction with the water flow, the pressure distribution on the left and right surfaces of the bionic tentacle becomes nonuniform. This pressure difference fluctuates periodically over time, giving rise to cyclic lateral oscillations of the bionic tentacle.

The deformation of the tentacle tip in the *X*-axis direction between the simulation and experimental results are compared, which show a very close match, although the deformation in the experimental setup is slightly larger than that observed in the simulation. This discrepancy arises due to the use of a rigid outer shell in the physical tentacle, which amplifies the deformation. The comparison validates the effectiveness of our FSI simulation method. The results indicate that the flexible bionic tentacle effectively translates water flow information into geometric deformation information of the elastic material. Deformation and displacement of the tentacle correlate positively with water flow speed, notably displaying substantial displacement along the incoming water flow direction (i.e., *X*-axis), along with oscillations along its tangential direction (i.e., *Z*-axis). Minimal variation in displacement and deformation is observed along the *Y*-axis. Consequently, water flow information can be indirectly acquired by monitoring the geometric deformation of the flexible bionic tentacle.

IV. Water Flow Perception Method Based on CNN-LSTM

Once the water flow information is converted into deformation information, it is captured as a 2-D image sequence by FlowSight's internal high-resolution camera. Traditional visual processing algorithms analyze contact surface deformation mainly by calculating the changes of feature points from their initial positions to estimate the external force applied [25]. However, these methods require high precision and have low generalizability when extracting the feature points. The underwater environments with complex and harsh working conditions might cause sensor to vibrate and leads to the drift of camera perspective, resulting in increased errors in the calculated positions of feature points. Moreover, relying solely on feature point positions may lead to the omission of certain information, such as variations in shadow area and the shape of features across the entire fluid-solid contact surface. Deep neural networks have been widely applied in image feature extraction [26]. Therefore, the water flow perception method is proposed using deep neural networks in this article. CNN has been widely used in image processing [27] and have the advantage of "translation invariance," enabling direct feature learning from samples without the need for complex feature extraction [28]. LSTM network is widely used in time series feature extraction [29].

In this section, the CNN is employed to extract features from each frame of the image sequence. Moreover, it is evident that the motion of the flexible bionic tentacle exhibits temporal patterns, and higher flow speed cause larger oscillation in the tangential direction of the water flow. To effectively utilize the temporal information, the LSTM network is used to process the flow characteristics in the timing sequence. Based on CNN-LSTM, the water flow perception method is proposed to extract the features of obtained visual image sequence, and simultaneously estimate the speed and direction of local water flow.

A. Problem Statement

In water flow, the flexible bionic tentacle undergoes deformation and deflection, as illustrated in Fig. 11(a). The geometric deformation of the elastic material induces changes in image features at the bottom of the silicone rubber layer, depicted in Fig. 11(b). Due to the protruding structure of the designed tentacle and the limited internal light intensity, the LED strip fails to illuminate the interior of the protruding tentacle. Consequently, a circular shadow forms in the center of the tentacle, as depicted in Fig. 11(c), effectively converting the geometric deformation of the tentacle into image features. As the water flow acts on the tentacle, the hard cap drives the tentacle to deflect, causing the shadow to move and change accordingly, as shown in Fig. 11(d). The greater the water flow speed, the larger the deviation of the bionic tentacle. Therefore, the water flow information should be extracted from the changed image features by the water flow perception neural network.

The real-time 2-D image sequence X_{img} captured by the internal camera serves as the input to the perception network. Subsequently, the network provides estimates for the water flow speed u_{flow} and direction ψ_{flow} denoted as $\hat{u}$flow and $\hat{\psi}$flow, correspondingly. The water flow perception task is formulated

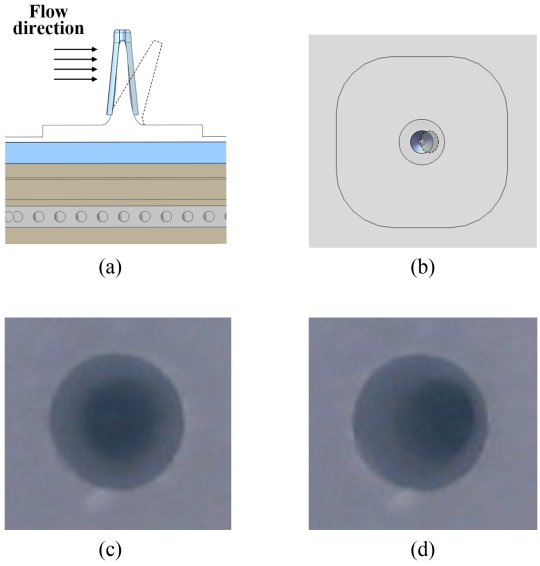

Fig. 11. Structure diagram of FlowSight's sensing principle and images captured by the internal camera. (a) Side sectional view. (b) Internal top view. (c) Captured image when there is no water flow. (d) Captured image after the water flow acts on the tentacle.

as a regression problem, expressed as follows:

$$\begin{cases} \hat{y} = \mathcal{F}_{\text{flow}}(X_{\text{img}}) \\ \quad = \left[\cos(\hat{\psi}_{\text{flow}}), \sin(\hat{\psi}_{\text{flow}}), \hat{u}_{\text{flow}}\right] \\ X_{\text{img}} = \{x^1_{\text{img}}, \ldots, x^i_{\text{img}}, \ldots, x^t_{\text{img}}\} \\ \quad x^i_{\text{img}} \in \mathbb{R}^{100\times100\times3}, i = 1, \ldots, t \end{cases} \tag{14}$$

where $\mathcal{F}_{\text{flow}}$ denotes the water flow perception network. x^i_{img} represents the ith image of the 2-D image sequence X_{img}, where each temporal sequence data contains t frames of image data. To mitigate computational complexity, preprocessing involves cropping each frame of the high-resolution images captured by the camera to retain solely the (100×100)-pixel region surrounding the tentacle, depicted in Fig. 11(c). The network output $\hat{y}$ includes the estimated flow speed information $\hat{u}_{\text{flow}}$ and flow direction information $\hat{\psi}_{\text{flow}}$. It is noteworthy that the flow direction ψ_{flow} undergoes processing via trigonometric functions $[\cos(\psi_{\text{flow}}), \sin(\psi_{\text{flow}})]$ to mitigate periodicity issues associated with angles. This conversion translates angle information into a 2-D vector representation, utilizing cosine and sine functions to represent angles, thereby facilitating computation. Meanwhile, the flow speed u_{flow} undergoes normalization processing in practical applications.

The water flow perception is defined as a regression problem, wherein the standard mean square error function serves as the loss function $\mathcal{L}$, expressed as follows:

$$\mathcal{L} = \frac{1}{n} \cdot \sum_{i=1}^{n} (y_i - \hat{y}_i)^2 \tag{15}$$

where y_i is the actual value of water flow.

As illustrated in Fig. 12, the CNN-LSTM based water flow perception network $\mathcal{F}_{\text{flow}}$ is designed to estimate flow speed and direction simultaneously, where CNN represents the convolutional neural network, FC denotes the fully connected layer, and LSTM refers to the LSTM network. Each captured image x^i_{img} of the image sequence X_{img} is input to convolutional layers at each time step. Through two CNN layers and an FC layer, the image features for each image sequence are extracted. Subsequently, the image features from each time step are inputted into the LSTM network to capture temporal sequence features. Finally, the estimated parameters $\hat{y}$ are output via an FC layer.

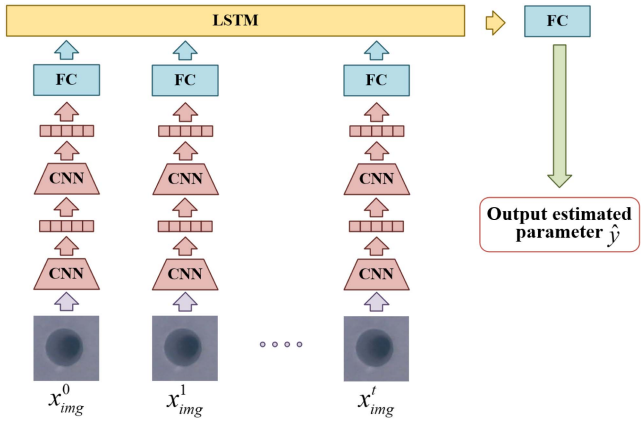

Fig. 12. Structure diagram of the water flow perception network.

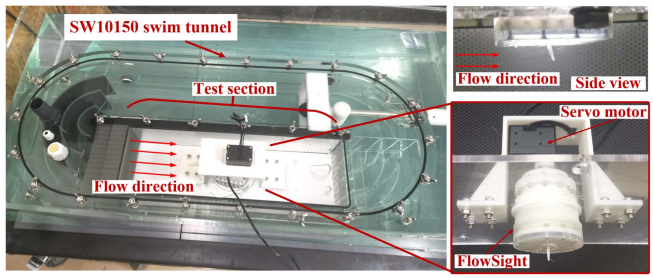

Fig. 13. Platform for data collection and experiments.

B. Dataset Collection and Production

The datasets are gathered and prepared for training and testing the water flow perception network in actual underwater environments. To facilitate data collection and experimentation with the FlowSight sensor in real-world scenarios, we developed the FlowSight experimental platform utilizing the SW10150 swim tunnel from Loligo Systems [30], depicted in Fig. 13. The SW10150 swim tunnel is capable of producing a consistently directed and uniform water flow within the $(46 \times 14 \times 14)$ cm test area, enabling flow speed adjustments ranging from 0.05 m/s to 1.75 m/s. The FlowSight is affixed to the cover plate and positioned at the center of the test area. Sealing rings are employed to maintain relative sealing and independence of the test area, as illustrated in the side view of Fig. 13, ensuring that the bionic tentacle faces the water flow. As the flow direction within the swim tunnel's test area remains fixed, a digital servo motor adjusts the direction of the FlowSight sensor, enabling

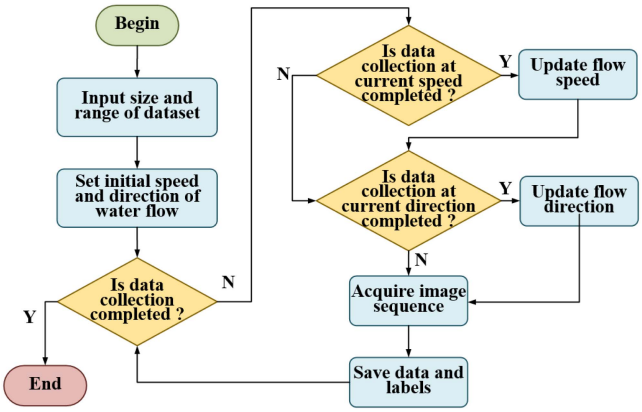

Fig. 14. Flow diagram of the automated data acquisition program.

variations in the sensor's relative orientation to the water flow, facilitating data collection across diverse flow directions.

The upper computer transmits the desired water flow speed to the SW10150 swim tunnel controller using Bluetooth communication, thus producing a uniform water flow with a velocity of u_{flow} within the test area. The desired angle is sent to the digital servo motor through a universal asynchronous receiver/transmitter (UART) serial port by the upper computer. In addition, the digital servo motor swiftly adjusts the orientation of the FlowSight sensor to the desired angle, establishing the relative angle between the water flow and the sensor as the water flow direction ψ_{flow}. Consequently, the upper computer can regulate both the speed u_{flow} and direction ψ_{flow} of the uniform flow, serving as the truth data for dataset collection purposes. The speed u_{flow} and direction ψ_{flow} information are logged as data labels associated with the corresponding image. The real-time image information captured by the internal camera of the FlowSight is transmitted to the upper computer via universal serial bus (USB) communication.

An automated data acquisition program is developed to streamline dataset collection, depicted in Fig. 14. First, the dataset size and collection range are specified. Subsequently, the initial water flow speed and direction are configured via the upper computer. The internal camera captures 2-D image data depicting silicone rubber surface deformation. After capturing one set of image sequence, the data labels including flow speed u_{flow} and direction ψ_{flow} are logged and stored on the upper computer. Subsequently, while maintaining the current flow speed, the digital servo motor is manipulated to alter the direction, indirectly modifying the water flow direction. Then, the dataset collection for the subsequent set continues. The water flow direction is continuously adjusted until the desired flow direction data is attained. Following this, the water flow speed is updated by the swim tunnel controller. The dataset collection resumes under the new water flow speed, with adjustments made to the water flow direction until the entire dataset is collected.

Considering the operational conditions and swimming velocity of the RoboDact, the water flow speed range was established from 32.5 cm/s to 71.5 cm/s, with increments of 3.25 cm/s, encompassing a total of 12 distinct speed tiers. Employing the aforementioned automated data acquisition program, a total of (12×32) datasets were gathered within the SW10150 swim tunnel for training purposes. In total, 12 distinct water flow speeds were configured. At each flow speed level, 32 datasets with randomly selected water flow directions were collected. Each dataset comprises 500 frames of 100×100 pixel chromatic sequence images, captured at a frame rate of 20 frames per second.

V. Experiment and Analysis

In this section, two quantitative tests are carried out to verify the effectiveness of the deformation model. Moreover, to evaluate the feasibility of the FlowSight design and confirm the effectiveness of the CNN-LSTM-based water flow perception method, the developed FlowSight sensor is employed to perform concurrent estimation of flow speed and direction in a controllable velocity swim tunnel. In addition, a motion control experiment of the RoboDact based on water flow perception is conducted.

A. Tests of the Deformation Model

In the initial test, a force sensor with a resolution of 0.0001 N is horizontally secured onto a vise, as shown in Fig. 15. The FlowSight sensor is mounted on a mobile platform capable of unidirectional movement along the horizontal plane. The FlowSight is randomly moved back and forth in the horizontal direction through the mobile platform. Therefore, the tentacle undergoes deformation upon contact with the force sensor. Throughout each measurement, the FlowSight is displaced by a random distance. Once the tentacle stabilizes, the force sensor measures the deformation restoring force F_e, while a stationary external camera records the tentacle's deformation. Following image acquisition, the deflection angles are marked and measured. Therefore, the restoring torque M_e, exerted on the tentacles' base, is indirectly computed as $M_e = F_e \cdot L_1$ by gauging the force sensor's reading F_e, where $L_1 = 1.9$ mm denotes the equivalent force arm. The deflection angle θ of the deformed tentacle is determined using computer-aided design software. The relationship between deflection angle θ and restoring torque M_e is shown in Fig. 16. It can be observed that the deflection of the tentacle is significantly linearly related to the applied torque with $R^2 = 0.9736$. And $M_e = 0.0324 \cdot \theta$. According to (8), $M_e = S \cdot \theta$. The torsional spring constant S is estimated as $\hat{S}_1 = 3.24 \times 10^{-5}\text{Nm/rad}$.

In the second test scenario, the FlowSight sensor is affixed to the cover plate and positioned at the center of the SW10150 swim tunnel, depicted in Fig. 15. A uniform flow with a velocity of u_0 is induced within the test area, which can be changed by the swim tunnel controller via the upper computer. The FlowSight tentacle is completely immersed in water, undergoing deformation upon interaction with the water flow. Similarly, the deformation of the tentacle is captured by a stationary external camera, with the deflection angle θ of the deformed tentacle being marked and measured. The relationship between the water flow speed u_0 and the deflection angle θ of the tentacle is depicted in

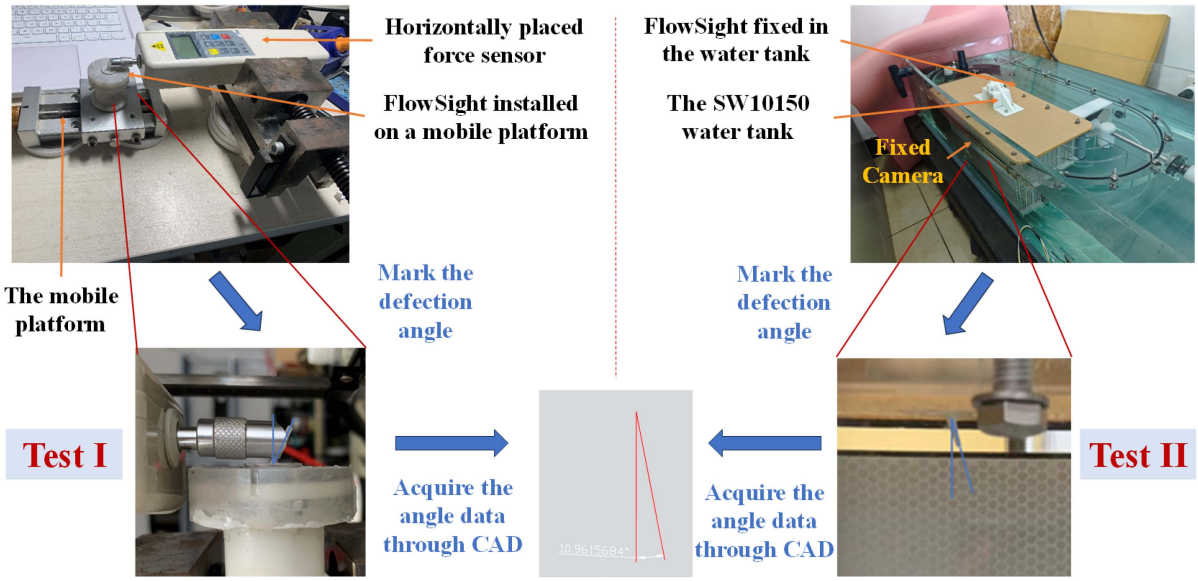

Fig. 15. Schematic diagram of the tentacle deformation and water flow tests.

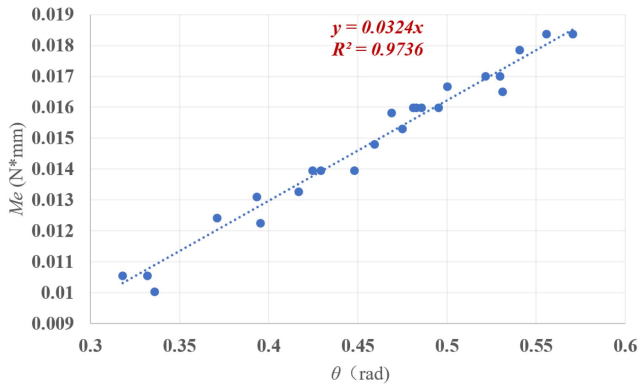

Fig. 16. Relationship between deflection angle θ and restoring torque M_e.

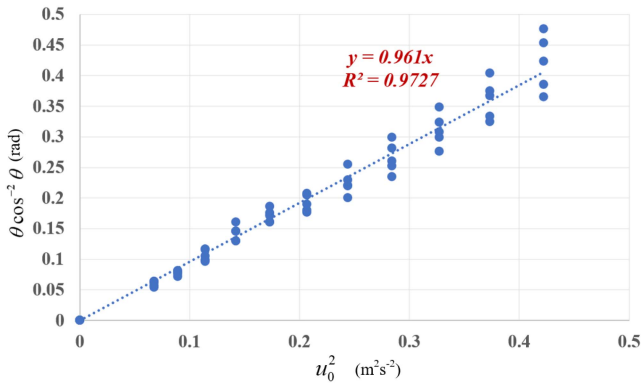

Fig. 17. Relationship between flow speed u_0 and deflection angle θ.

Fig. 17. Notably, it is observed that $\theta\cos^{-2}\theta$ exhibits a substantial linear relationship with u_0^2, yielding $R^2 = 0.9727$, which can be expressed as follows:

$$\frac{\theta}{\cos^2\theta} = 0.961u_0^2. \tag{16}$$

According to (9), the following can be obtained:

$$\frac{1}{4S}\rho C_D D L_p^2 = 0.961 \tag{17}$$

where average diameter of the tentacle is $D = 2.5$ mm, height of the tentacle is $L_p = 10$ mm, the water density is $\rho = 1000$ kg/m^3, and the dimensionless drag coefficient is $C_D = 0.52$. Therefore, the torsional spring constant S is estimated as $\hat{S}_2 = 3.38 \times 10^{-5}$Nm/rad.

The force sensor test reveals a linear correlation between tentacle deflection and applied torque in a stable state, aligning with the proposed deformation model of the tentacle. The swim tunnel test validates the correlation between tentacle deformation and water flow velocity. The estimated torsional spring constants $\hat{S}_1$ and $\hat{S}_2$ from both tests fall within the allowable range of error. The proposed tentacle deformation model proves to be effective.

B. Experiments of Flow Speed and Direction Estimation

Based on the dataset generated as described in Section IV, the training and testing sets were partitioned in a 9 : 1 ratio. The proposed water flow perception method based on CNN-LSTM was employed for training the perception network, with each timing sequence data containing 5 frames of image. Two control groups were trained separately using CNN and LSTM networks for perception network training. For the convenience of displaying the network of three methods, Table III delineates the feature size parameters for the outputs following each network layer.

The proposed CNN-LSTM-based perception method for synchronous estimation of flow speed and direction involves the following steps. The input timing sequence data traverses two

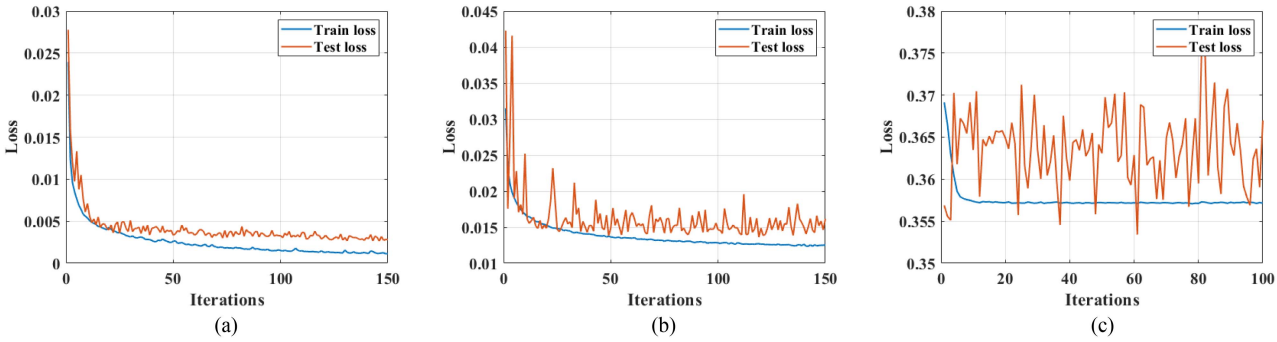

Fig. 18. Training processes of the perception network based on three methods. (a) CNN-LSTM. (b) CNN. (c) LSTM.

TABLE III
CHARACTERISTIC PARAMETERS OF EACH NETWORK LAYER OF THE THREE METHODS

Method	CNN-LSTM	CNN	LSTM
Input	$(5, 100, 100, 3)$	$(5, 100, 100, 3)$	$(5, 100, 100, 3)$
Conv. I	$(5, 98, 98, 16)$	$(5, 98, 98, 16)$	None
Pooling I	$(5, 49, 49, 16)$	$(5, 49, 49, 16)$	None
Conv. II	$(5, 47, 47, 32)$	$(5, 47, 47, 32)$	None
Pooling II	$(5, 23, 23, 32)$	$(5, 23, 23, 32)$	None
FC I	$(5, 64)$	(5×64)	$(5, 100 \times 100 \times 3)$
LSTM	(64)	None	(64)
FC II	None	(5×16)	None
FC III	(3)	(3)	(3)

TABLE IV
MEASUREMENT ERROR OF THE THREE METHODS IN THE TEST SET

Method	CNN-LSTM	CNN	LSTM
MAE of speed (cm/s)	1.1903	2.1709	10.6449
Relative error of speed	3.05%	5.57%	27.29%
STD of speed (cm/s)	1.5967	3.0402	12.5219
MAE of direction (°)	3.5407	6.1202	191.4510
Relative error of direction	0.98%	1.70%	53.18%
STD of direction (°)	4.84	9.7219	88.4898

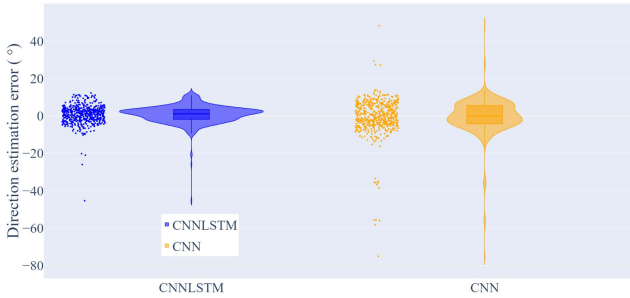

Fig. 19. Distributions of flow direction estimation error using CNN-LSTM and CNN methods.

sets of convolutional layers and average pooling layers (with a 3×3 convolutional kernel size and a stride of 1), yielding an output image feature size of $(5, 23, 23, 32)$. Subsequently, it passes through a feature encoding fully connected layer, resulting in an output image feature size of $(5, 64)$, wherein each frame's image is encapsulated into a $(1, 64)$ array feature, encompassing a total of 5 frames. The LSTM network sequentially processes the features of each frame. Finally, a regression analysis is conducted using a fully connected layer to generate a three-dimensional estimate of flow speed $\hat{u}$ and direction $\hat{\psi}$. When utilizing the CNN exclusively, the identical CNN employed in CNN-LSTM is utilized. The input timing sequence of image features is extracted as $(5, 23, 23, 32)$. Subsequently, these features undergo direct processing through two fully connected layers. Then, the network outputs a 3-D estimate of flow speed and direction. Similarly, in the case of employing the LSTM network exclusively, the identical LSTM network utilized in CNN-LSTM is employed. However, there is no image feature extraction step involved. Instead, each image frame is directly flattened into a 1-D array of size $(1, 100 \times 100 \times 3)$. Subsequently, the LSTM network sequentially processes each image frame, culminating in the network producing a 3-D estimate of flow speed and direction through a regression fully connected layer.

Subsequently, the three methods are individually trained using same training parameters (learning rate of 0.01 and batch size of 16). The training processes of the perception network based on these methods are illustrated in Fig. 18. When employing the proposed water flow perception method based on CNN-LSTM, the loss steadily converges throughout the training process. After 150 iterations, the losses of both the CNN and CNN-LSTM networks exhibit gradual decline and convergence, whereas the loss of the LSTM network fails to converge.

To further validate the effectiveness and generalizability of the three methods, a testing set comprising 38 distinct flow speeds and directions was collected to assess the performance of the three trained networks. Table IV illustrates the parameter estimation errors for each method, including the mean absolute error (MAE), standard deviation (STD), and relative error for both water flow speed and direction. The relative error was computed by dividing the MAE by the data distribution range, which represents the difference between the maximum and minimum true values in the dataset.

In addition, the testing error distributions of the three methods are depicted in Figs. 19–21. It is evident that the error distribution area of the CNN-LSTM model is more tightly concentrated, with smaller error values. Conversely, the error

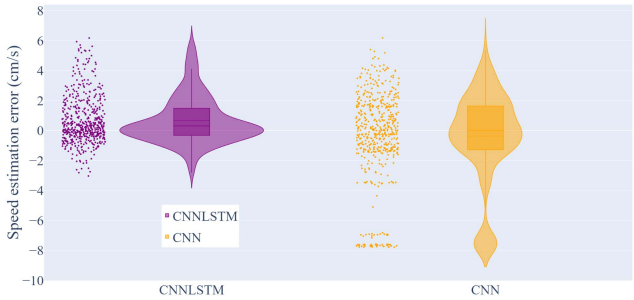

Fig. 20. Distributions of flow speed estimation error using CNN-LSTM and CNN methods.

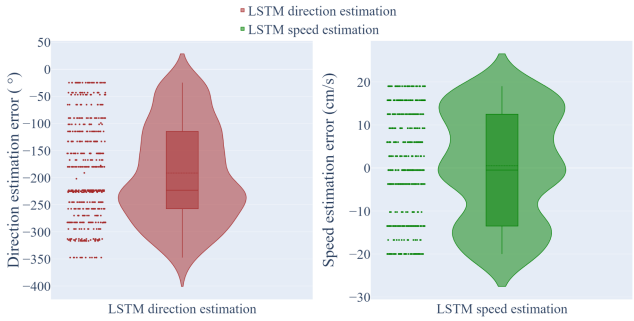

Fig. 21. Distributions of water flow estimation error using LSTM method.

distribution area of the CNN model is broader, and the error value is larger. Notably, the LSTM model demonstrates an inability to accurately predict numerical values, characterized by extensive error distributions and disparities.

The test results of these methods are illustrated in Fig. 22. Utilizing the CNN-LSTM model, the average absolute error for water flow speed measurement in the swim tunnel is 1.1903 cm/s, with a relative error of 3.05%. Similarly, for water flow direction measurement, the average absolute error is 3.5407°, with a relative error of 0.98%. The test results, depicted in Fig. 22(a) and (d), highlight the effectiveness of the CNN-LSTM network in simultaneous estimation of water flow speed and direction. At high water flow speeds, the bionic tentacle experiences increased vibration amplitude and frequency in the direction that is tangential to the incoming flow. Consequently, the tentacle encounters more irregular disturbances, leading to decreased stability of image features and increased estimation error of the flow speed.

Utilizing the CNN alone for feature extraction, followed by a fully connected network, enables effective synchronous estimation of flow speed and direction. The average absolute error for flow speed is 2.1709 cm/s, with a relative error of 5.57%. Similarly, for flow direction measurement, the average absolute error is 6.1202°, with a relative error of 1.70%. The test results are shown in Fig. 22(b) and (e). Nevertheless, due to minimal changes in image features at low speeds, temporal sequence information remains unextracted, leading to a decline in flow speed perception accuracy. Furthermore, as water flow speed and tentacle vibration amplitude and frequency escalate, the efficacy of flow speed measurement markedly declines. The absence of temporal feature extraction by the network exacerbates perception accuracy reduction.

When employing the LSTM network directly to train image data, the relative errors for water flow speed and direction are 27.29% and 53.18%, respectively. The test results are depicted in Fig. 22(c) and (f), which exhibit nearly straight-line estimated values for water flow speed and direction, suggesting ineffective measurements. The direct flattening of 2-D images into 1-D arrays, inputted into the LSTM network without feature extraction, hinders network convergence, resulting in ineffective estimation of water flow speed and direction.

Based on the above experiments and comparisons, the CNN-LSTM network has exhibited the best performance. While the CNN model can discern flow speed and direction based on vibration information when sensor deformation changes are subtle, the incorporation of the time series network adds even more valuable information to the estimation process. Therefore, the CNN-LSTM model integrates temporal information from the image sequence when estimating the flow speed and direction. Through the utilization of the CNN for feature extraction followed by the LSTM network for temporal information extraction, the estimation of flow speed and direction is notably enhanced. It validates the effectiveness of the proposed CNN-LSTM-based water flow perception method, demonstrating FlowSight's capability for simultaneous measurement of water flow speed and direction. Specifically, the average absolute error for flow speed measurement is 1.1903 cm/s with a relative error of 3.05%, while the average absolute error for flow direction measurement is 3.5407° with a relative error of 0.98%.

The measurement error of FlowSight, which is within a range of 3.05%, primarily arises from two factors. First, the dataset collected by the sensor inherently contains a certain degree of error due to limitations in the precision of the tentacles and the detection system. Second, environmental disturbances in the experimental setup, such as turbulence and bubbles in the flow field, introduce additional noise and inaccuracies in the measurements. These factors collectively limit the current accuracy of the sensor. As noted, the sensors' performance is currently constrained within a specific flow speed range due to inherent challenges. At lower flow speeds, the deformation characteristics of the flexible tentacles are not sufficiently pronounced, leading to reduced detection accuracy. At higher flow speeds, the flow field generated by our experimental setup contains a significant number of bubbles and turbulence, resulting in disturbances and increased measurement errors for the tentacles. To address these challenges and further improve the accuracy of FlowSight, we propose the following directions for future research. By constructing a FlowSight sensor equipped with an array of flexible tentacles, we aim to increase the number of detectable deformation features. This enhancement will provide a richer dataset and improve the robustness of the sensor in capturing complex flow dynamics, thereby reducing measurement error. Increasing the size and diversity of the dataset used for calibration and algorithm training will help improve the precision of the sensor. A larger dataset will enable better generalization of the machine learning models used for flow speed and direction

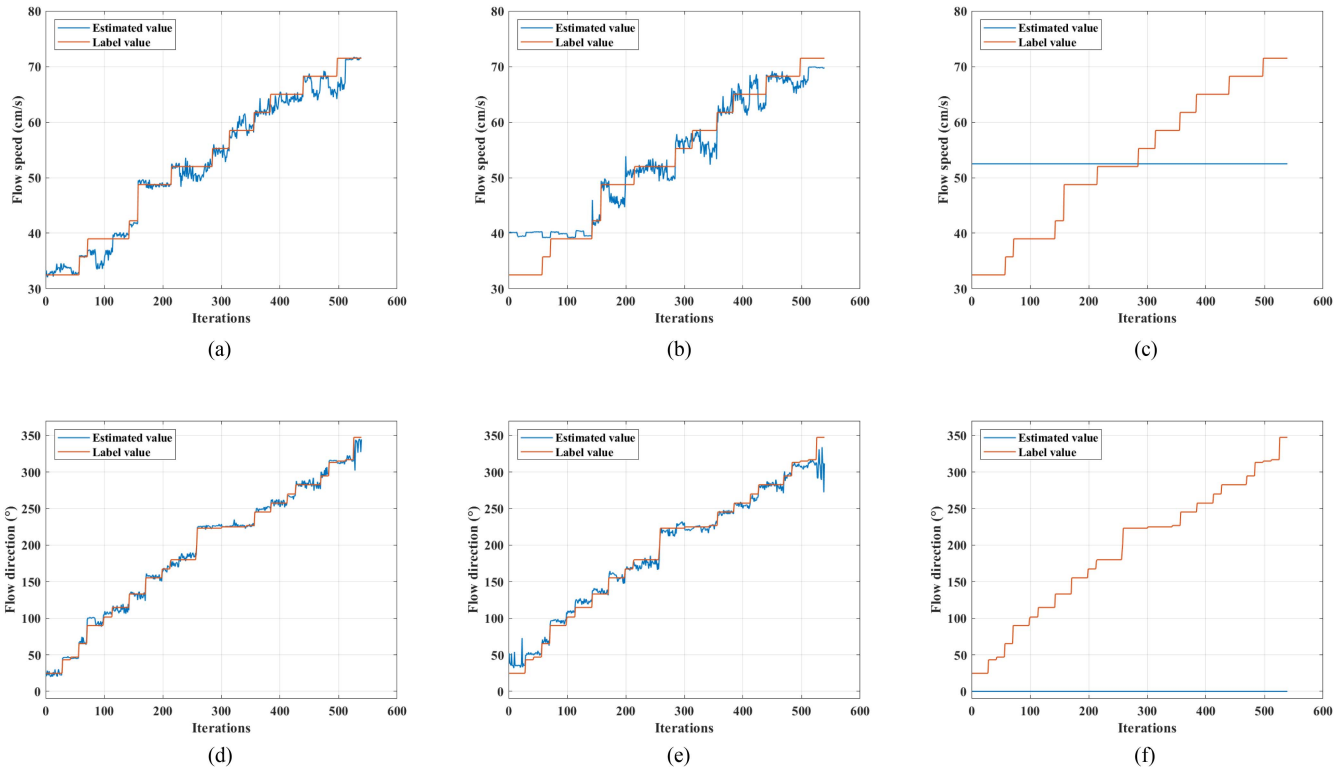

Fig. 22. Test results of the three methods in the test set. (a) Speed measurement with CNN-LSTM. (b) Speed measurement with CNN. (c) Speed measurement with LSTM. (d) Direction measurement with CNN-LSTM. (e) Direction measurement with CNN. (f) Direction measurement with LSTM.

estimation, leading to more accurate predictions and reduced errors.

C. Closed-Loop Motion Control Experiment Based on Water Flow Perception

By integrating the developed FlowSight sensor, the water flow perception ability of the RoboDact can be improved. The RoboDact can discern its speed and direction relative to the water flow, enabling it to adapt to the complex underwater environment. Therefore, a closed-loop motion control experiment based on water flow perception is devised to show the application performance of the FlowSight sensor.

The framework of the motion control system for the RoboDact based on water flow perception is delineated in Fig. 23. Initially, the FlowSight sensor is harnessed to concurrently estimate the flow speed and direction. After obtaining the water flow information, a fuzzy PID controller [31] is employed to perform closed-loop motion control based on errors of the current and desired motion state. Finally, the swimming gait is dynamically generated in real-time by the lower level fin drive network, propelling the motion of the RoboDact.

In the closed-loop motion control experiment, the RoboDact is controlled to turn in the opposite direction of the water flow and swim forward along that direction to simulate the counterflow swimming behavior of fish. In the experiment, the desired angle ψ_g is set to $180°$. The RoboDact can estimate its relative angle ψ_{flow} with the water flow and calculate the error of the desired

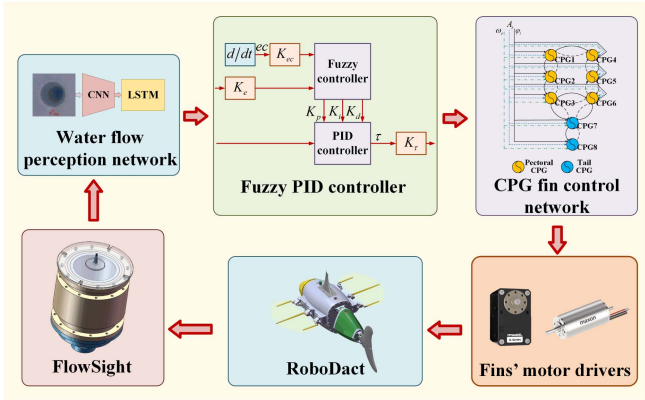

Fig. 23. Framework of the motion control system based on water flow perception.

angle $\Delta\psi = \psi_g - \psi_{\text{flow}}$. The fuzzy PID controller continuously calculates and outputs the control law τ_{flow} based on the error $\Delta\psi$, which is then used by the lower level fin drive network to control the movement of each fin. The lower level fin drive network is designed based on central pattern generator (CPG) in our previous works [32]. To simplify the computation, the CPG amplitude and phase difference of each fin are fixed. τ_{flow} is used as differential signal to adjust the difference of undulatory frequency between two pectoral fins of the RoboDact, which can generate the yaw moment and change course of the RoboDact.

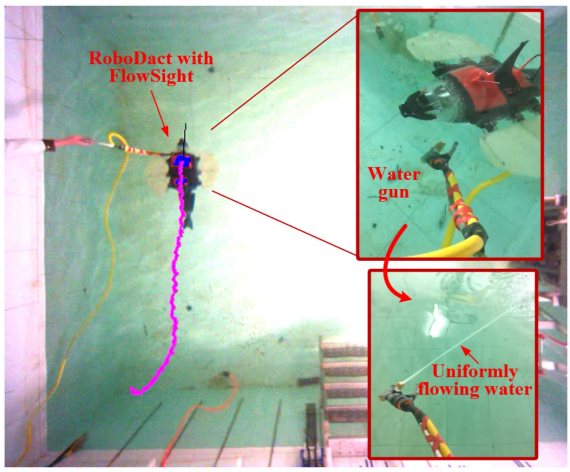

Fig. 24. Schematic diagram of the closed-loop motion control experiment based on flow perception.

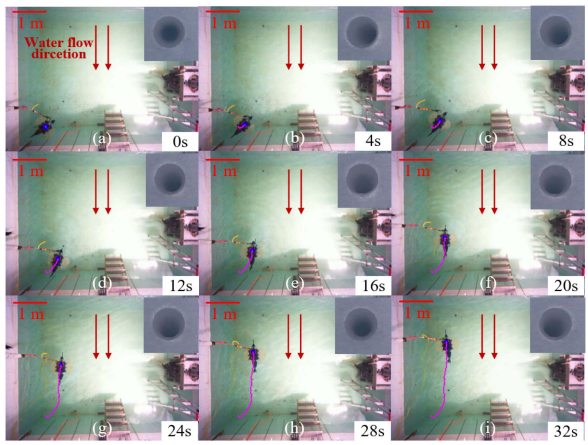

Fig. 25. Snapshot sequence of the closed-loop motion control experiment based on flow perception.

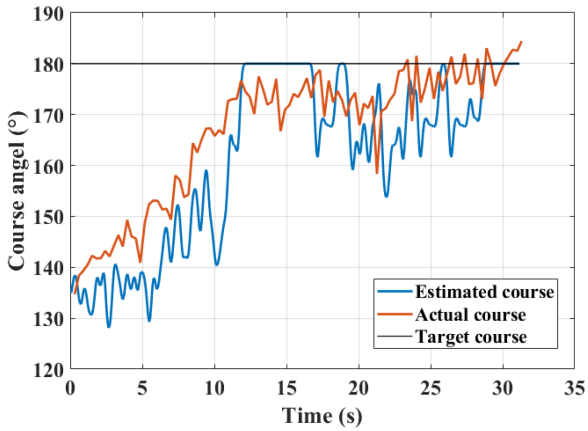

Fig. 26. Course change curve of the RoboDact in the closed-loop motion control experiment based on flow perception.

The undulatory frequency of the fins is calculated as follows:

$$\begin{cases} f = & [f_L, f_R, f_T]^T \\ f_L = & f_0 + k_{\text{flow}} \cdot \tau_{\text{flow}} \\ f_R = & f_0 - k_{\text{flow}} \cdot \tau_{\text{flow}} \\ f_T = & 0 \end{cases} \tag{18}$$

where k_{flow} represents the proportionality coefficient, and f_L and f_R are the undulatory frequencies of the left and right pectoral fins, respectively. The tail fin motion frequency f_T is set to 0 to suppress any disturbances to the course of the RoboDact caused by the tail fin motion. $f_0 > 1$ Hz to ensure that the pectoral fins can generate sufficient forward thrust for the counterflow swimming behavior.

As depicted in Fig. 24, the motion control experiment is conducted in an indoor swim pool with dimensions of $(5 \times 4 \times 1.1)$ m. Given constraints in facility conditions, establishing a large-scale uniformly flowing field with a constant direction for counterflow swimming of the RoboDact is challenging. Consequently, a high-pressure water gun is employed to generate a small-scale uniformly water flow, mimicking the desired conditions. The high-pressure water gun is fixed in a designated direction, aligning the water flow with the measurement area of the FlowSight to emulate the sensing scenario in a uniformly flowing field. Moreover, the tail fin remains stationary to prevent excessive swinging of the RoboDact, which may cause difficulty in aligning the water flow with the sensor. Control over the RoboDact's turning and counterflow swimming is exclusively exerted through the undulation of the two side pectoral fins. In instances where the FlowSight sensor fails to detect stable water flow, the estimated value is adopted as the desired course. Consequently, the movement of the RoboDact is attenuated, facilitating adjustment of the high-pressure water gun's position to enable the FlowSight to measure the water flow and resume the experiment seamlessly.

The trained perception network is deployed on the edge computing module, NVIDIA Jetson Orin NX in the RoboDact prototype. The response time of FlowSight sensor is set at 50 ms. To make the sensor more robust, the closed-loop control system operates with a control cycle of 100 ms. Initially, the RoboDact maintains a certain angle relative to the water flow direction. Subsequently, the robot turns to orient itself toward the direction of the water flow, gradually increasing the relative angle between the robot and the water flow until it reaches $180°$. Thereafter, the RoboDact maintains this direction and proceeds to swim forward. A global vision system is developed to capture real-time images of the entire swimming pool, as illustrated in Fig. 25. Based on the water flow perception, the RoboDact successfully completes the closed-loop motion control tasks. The water flow direction is depicted from top to bottom, with the images in the upper right corners of each subfigure representing the 2-D images captured by the FlowSight's internal camera.

Throughout the experiment, as the water flow direction remains constant, the relative angle of the RoboDact with respect to the water flow can be calculated using the water flow perception network. The variations of the course angle estimated by the FlowSight sensor and the global vision system are shown in Fig. 26. The course angle of the RoboDact in the world coordinate system is calculated through the known water flow direction and the estimated direction of the FlowSight, which is

indicated as the estimated course. Furthermore, the course angle can also be measured using the global vision system, expressed as the actual course. After perceiving the flow direction, the RoboDact is directed by the motion control system to turn left. From 0 s to 12.3 s, the robot turns toward the desired course. From 12.3 s to 32 s, the RoboDact maintains the desired course and swims from the bottom to the top of the water pool in the opposite direction of the flow. The RoboDact can sense the water flow speed and direction, enabling swift turning and swimming against the flow. This substantiates the feasibility of the developed FlowSight sensor and the effectiveness of the proposed water flow perception method.

VI. Conclusion

In this article, a novel vision-based ALL sensor FlowSight was developed, inspired by the lateral line neuromast of fishes. FlowSight allows for simultaneous sensing speed and direction of local water flow, thereby enhancing the underwater perception capabilities of underwater robots. A flexible bionic tentacle made of silicone rubber was designed to sense water flow. The motion characteristics of the tentacle were analyzed through FSI simulation, and a deformation model of the tentacle was developed and tested. The tentacle undergoes deformation upon contact with water flow, converting water flow information into elastic deformation information. This deformation is captured and transformed into 2-D image data by an internal camera within the FlowSight. A CNN-LSTM based water flow perception method was proposed to extract flow speed and direction from the captured image sequence. The CNN extracts image features, while the LSTM network is employed to extract timing sequence features. Subsequently, a dataset was collected and produced through actual experiments in a controllable swim tunnel, which was utilized to train and test the water flow perception network. Finally, utilizing the developed FlowSight and RoboDact prototypes, a closed-loop motion control experiment based on water flow perception was conducted to simulate the counterflow swimming behavior of fish. The experimental results demonstrated the feasibility of the developed bionic ALL sensor FlowSight and the effectiveness of the proposed water flow perception method.

In future work, our attention will be directed toward three aspects. First, we aim to design an enhanced version of FlowSight featuring multiple bionic tentacles. This advancement will enable the extension of local water flow perception to encompass flow field perception. By doing so, we aspire to estimate the high-resolution 2-D vector distribution of the flow field. Moreover, we will explore the application of alternative imaging techniques on sensors to improve sensor performance. For example, event-based cameras and other vision sensors with low-delay and high-time resolution are used for tentacle deformation feature detection and water flow sensing. Finally, we plan to expand the flow speed detection range of FlowSight, thereby enhancing its reliability during robotic task execution. The research will focus on two key directions: optimizing the diameter of the tentacles and improving the experimental setup. The developed FlowSight will also be subject to rigorous testing in wild environments. This will serve to evaluate its measurement performance and enhance its robustness and applicability in the face of varying natural water flow conditions. The RoboDact can undertake more intelligent underwater tasks effectively.

References

[1] Y. Jiang, Z. Ma, and D. Zhang, "Flow field perception based on the fish lateral line system," *Bioinspiration Biomimetics*, vol. 14, no. 4, 2019, Art. no. 041001.

[2] T. Kim, J. Kim, and S.-C. Yu, "Development of bioinspired multimodal underwater robot "HERO-BLUE" for walking, swimming, and crawling," *IEEE Trans. Robot.*, vol. 40, pp. 1421–1438, 2024.

[3] X. Zheng, W. Wang, M. Xiong, and G. Xie, "Online state estimation of a fin-actuated underwater robot using artificial lateral line system," *IEEE Trans. Robot.*, vol. 36, no. 2, pp. 472–487, Apr. 2020.

[4] Y. Zhong, Z. Hong, Y. Li, and J. Yu, "A general kinematic model of fish locomotion enables robot fish to master multiple swimming motions," *IEEE Trans. Robot.*, vol. 40, pp. 750–763, 2024.

[5] T. J. Pitcher, B. L. Partridge, and C. S. Wardle, "A blind fish can school," *Science*, vol. 194, no. 4268, pp. 963–965, Nov. 1976.

[6] J. F. Webb, "Morphological diversity, development, and evolution of the mechanosensory lateral line system," in *The Lateral Line System*, vol. 48. New York, NY, USA: Springer, 2013, pp. 17–72.

[7] H. Bleckmann and R. Zelick, "Lateral line system of fish," *Integrative Zool.*, vol. 4, no. 1, pp. 13–25, 2009.

[8] Z. Zhang, C. Zhou, L. Cheng, X. Wang, and M. Tan, "Real-time velocity vector resolving of artificial lateral line array with fishlike motion noise suppression," *IEEE Trans. Robot.*, vol. 39, no. 6, pp. 4350–4365, Dec. 2023.

[9] Z. Han et al., "Artificial hair-like sensors inspired from nature: A review," *J. Bionic Eng.*, vol. 15, no. 3, pp. 409–434, May 2018.

[10] Y. Yang et al., "Artificial lateral line with biomimetic neuromasts to emulate fish sensing," *Bioinspiration Biomimetics*, vol. 5, Mar. 2010, Art. no. 16001.

[11] C. Abels, A. Qualtieri, M. D. Vittorio, W. M. Megill, and F. Rizzi, "A bio-inspired real-time capable artificial lateral line system for freestream flow measurements," *Bioinspiration Biomimetics*, vol. 11, no. 3, Jun. 2016, Art. no. 035006.

[12] B. J. Wolf, J. A. S. Morton, W. N. MacPherson, and S. M. v. Netten, "Bio-inspired all-optical artificial neuromast for 2D flow sensing," *Bioinspiration Biomimetics*, vol. 13, no. 2, Feb. 2018, Art. no. 026013.

[13] J. F. Fuentes-Pérez, C. Meurer, J. A. Tuhtan, and M. Kruusmaa, "Differential pressure sensors for underwater speedometry in variable velocity and acceleration conditions," *IEEE J. Ocean. Eng.*, vol. 43, no. 2, pp. 418–426, Apr. 2018.

[14] Y. Zhu et al., "Research on the direction perception of cruising copepods by the fish lateral line using pressure difference matrix and residual neural network regression method," *Ocean Eng.*, vol. 292, Jan. 2024, Art. no. 116497.

[15] A. T. Abdulsadda and X. Tan, "Underwater source localization using an IPMC-based artificial lateral line," in *Proc. 2011 IEEE Int. Conf. Robot. Automat.*, May 2011, pp. 2719–2724.

[16] Y. Liu, M. Klaas, and W. Schröder, "Measurements of the wall-shear stress distribution in turbulent channel flow using the micro-pillar shear stress sensor MPS 3," *Exp. Thermal Fluid Sci.*, vol. 106, pp. 171–182, Sep. 2019.

[17] B. J. Wolf and S. M. V. Netten, "Hydrodynamic imaging using an all-optical 2D artificial lateral line," in *Proc. 2019 IEEE Sensors Appl. Symp. (SAS)*, Sophia Antipolis, France: IEEE, Mar. 2019, pp. 1–6.

[18] T. Zhang, R. Wang, Y. Wang, L. Cheng, S. Wang, and M. Tan, "Design and locomotion control of a dactylopteridae-inspired biomimetic underwater vehicle with hybrid propulsion," *IEEE Trans. Autom. Sci. Eng.*, vol. 19, no. 3, pp. 2054–2066, Jul. 2022.

[19] A. Nagiel, D. Andor-Ardó, and A. J. Hudspeth, "Specificity of afferent synapses onto plane-polarized hair cells in the posterior lateral line of the zebrafish," *J. Neurosci.: Official J. Soc. Neurosci.*, vol. 28, no. 34, pp. 8442–8453, Aug. 2008.

[20] J. A. Humphrey and F. G. Barth, "Medium Flow-Sensing Hairs: Biomechanics and Models," in *Advances in Insect Physiology*, vol. 34, Amsterdam, The Netherlands: Elsevier, 2007, pp. 1–80.

[21] H. Schlichting and K. Gersten, "Fundamentals of boundary–layer theory," in *Boundary-Layer Theory*, 9th ed. Berlin, Germany: Springer, 2017, pp. 29–33.

[22] M. J. McHenry, J. A. Strother, and S. M. V. Netten, "Mechanical filtering by the boundary layer and fluid–structure interaction in the superficial neuromast of the fish lateral line system," *J. Comp. Physiol. A*, vol. 194, no. 9, pp. 795–810, Sep. 2008.
[23] F. G. Barth, "How to catch the wind: Spider hairs specialized for sensing the movement of air," *Naturwissenschaften*, vol. 87, no. 2, pp. 51–58, Feb. 2000.
[24] X.-A. Han, Y. Ma, and X. Huang, "The cubic trigonometric Bézier curve with two shape parameters," *Appl. Math. Lett.*, vol. 22, no. 2, pp. 226–231, Feb. 2009.
[25] S. Cui, R. Wang, J. Hu, C. Zhang, L. Chen, and S. Wang, "Self-supervised contact geometry learning by GelStereo visuotactile sensing," *IEEE Trans. Instrum. Meas.*, vol. 71, 2021, Art. no. 5004609.
[26] Z.-Q. Zhao, P. Zheng, S.-T. Xu, and X. Wu, "Object detection with deep learning: A review," *IEEE Trans. Neural Netw. Learn. Syst.*, vol. 30, no. 11, pp. 3212–3232, Nov. 2019.
[27] Z. Li, F. Liu, W. Yang, S. Peng, and J. Zhou, "A survey of convolutional neural networks: Analysis, applications, and prospects," *IEEE Trans. Neural Netw. Learn. Syst.*, vol. 33, no. 12, pp. 6999–7019, Dec. 2022.
[28] J. Gu et al., "Recent advances in convolutional neural networks," *Pattern Recognit.*, vol. 77, pp. 354–377, 2018.
[29] Z. Zhang et al., "Wind speed prediction method using shared weight long short-term memory network and Gaussian process regression," *Appl. Energy*, vol. 247, pp. 270–284, 2019.
[30] S. Loligo, "Loligo systems swim tunnel overview," Accessed: Apr. 10, 2024. [Online]. Available: https://www.loligosystems.com/products/swim-tunnels/swim-tunnels/
[31] B. Hu, G. K. Mann, and R. G. Gosine, "New methodology for analytical and optimal design of fuzzy PID controllers," *IEEE Trans. Fuzzy Syst.*, vol. 7, no. 5, pp. 521–539, Oct. 1999.
[32] T. Zhang, R. Wang, S. Wang, Y. Wang, G. Zheng, and M. Tan, "Residual reinforcement learning for motion control of a bionic exploration robot—RoboDact," *IEEE Trans. Instrum. Meas.*, vol. 72, 2023, Art. no. 7504313.

Tiandong Zhang (Member, IEEE) received the B.E. degree in electronic science and technology from the Beijing University of Posts and Telecommunications, Beijing, China, in 2018, and the Ph.D. degree in control theory and control engineering from the Institute of Automation, Chinese Academy of Sciences (CASIA), Beijing, in 2023.

He is currently an Assistant Professor with the State Key Laboratory of Multimodal Artificial Intelligence Systems, Institute of Automation, Chinese Academy of Sciences. His research interests include intelligent control, biomimetic robots, and underwater perception.

Rui Wang (Senior Member, IEEE) received the B.E. degree in automation from the Beijing Institute of Technology, Beijing, China, in 2013, and the Ph.D. degree in control theory and control engineering from the Institute of Automation, Chinese Academy of Sciences (CASIA), Beijing, in 2018.

He is currently an Associate Professor with the State Key Laboratory of Multimodal Artificial Intelligence Systems, CASIA. His current research interests include intelligent control, robotics, underwater robots, and biomimetic robots. He has authored or coauthored more than 60 refereed journal, and conference papers, e.g., IEEE TRANSACTIONS ON SYSTEMS, MAN AND CYBERNETICS: SYSTEMS, IEEE TRANSACTIONS ON INDUSTRIAL ELECTRONICS, IEEE TRANSACTIONS ON AUTOMATION SCIENCE AND ENGINEERING, IEEE International Conference on Robotics and Automation, and IEEE Conference on Automation Science and Engineering.

Qiyuan Cao (Student Member, IEEE) received the B.E. degree in mechanical engineering from Shandong University, Jinan, China, in 2021. He is currently working toward the Ph.D. degree in control theory and control engineering with the State Key Laboratory of Multimodal Artificial Intelligence Systems, Institute of Automation, Chinese Academy of Sciences, Beijing, China.

His research interests include biomimetic robotics, deep reinforcement learning, and intelligent control.

Shaowei Cui (Member, IEEE) received the B.E. degree in process equipment and control engineering from the South China University of Technology, Guangzhou, China, in 2017, and the Ph.D. degree in pattern recognition and intelligent systems from the Institute of Automation, Chinese Academy of Sciences, Beijing, China, in 2022.

He is currently an Assistant Professor with the State Key Laboratory of Multimodal Artificial Intelligence Systems, Institute of Automation, Chinese Academy of Sciences. His current research interests include visuo-tactile perception and robotic dexterous manipulation.

Gang Zheng (Senior Member, IEEE) received the B.E. and M.E. degrees in communication and systems from Wuhan University, Wuhan, China, in 2001 and 2004, respectively, and the Ph.D. degree in automatic control from ENSEA, Cergy-Pontoise, France, in 2006.

Since 2007, he has held postdoctoral positions with INRIA Grenoble, with the Laboratoire Jean Kuntzmann, and with ENSEA. From September 2009, he has been a permanent Researcher with INRIA Lille, Villeneuve-d'Ascq, France. His research interests include control and observation of nonlinear systems, and its applications to rigid and soft robotics.

Shuo Wang (Member, IEEE) received the B.E. degree in electrical engineering from the Shenyang Architecture and Civil Engineering Institute, Shenyang, China, the M.E. degree in industrial automation from the Northeastern University, Shenyang, and the Ph.D. degree in control theory and control engineering from the Institute of Automation, Chinese Academy of Sciences, Beijing, China, in 1995, 1998, and 2001, respectively.

He is currently a Professor with the State Key Laboratory of Multimodal Artificial Intelligence Systems, Institute of Automation, Chinese Academy of Sciences. His research interests include biomimetic robot, underwater robot, and multirobot systems.